Journal of Nuclear Materials 430 (2012) 221–228

Contents lists available at SciVerse ScienceDirect

Journal of Nuclear Materials

journal homepage: www.elsevier.com/locate/jnucmat

Impact of thermal conductivity models on the coupling of heat transport and oxygen diffusion in UO_2 nuclear fuel elements

Bogdan Mihaila [a,*], Marius Stan [b], Justin Crapps [b]

[a] Materials Science and Technology Division, Los Alamos National Laboratory, Los Alamos, NM 87545, USA
[b] Nuclear Engineering Division, Argonne National Laboratory, Argonne, IL 60439, USA

ARTICLE INFO

Article history:
Received 9 December 2011
Accepted 4 July 2012
Available online 14 July 2012

ABSTRACT

We study the coupled thermal transport, oxygen diffusion, and thermal expansion of a generic nuclear fuel element consisting of a UO_2 fuel pellet and stainless steel cladding separated by a helium gap for the purpose of evaluating the impact of various thermal conductivity models on the predictions of the temperature profile and deformation. Using a series of steady-state and time-dependent finite-element simulations with a variety of initial- and boundary-value conditions, thermo-mechanical response of the fuel element is evaluated. The results show that including the deviation from stoichiometry, x, in the thermal conductivity model is paramount for obtaining accurate predictions in the centerline temperature and the extent of the radial deformation of the fuel pellet. In a surprising result, the coupling between the heat transport and the oxygen diffusion is relatively strong for small values of the fixed composition boundary conditions x_b, whereas the coupling becomes weaker for large values of x_b.

© 2012 Elsevier B.V. All rights reserved.

1. Introduction

Understanding the evolving properties of nuclear fuels and predicting the behavior of nuclear fuel elements (ceramic fuel pellets or metallic fuel rods) are major challenges for fuel manufacturing, performance, and storage. The quantitative description of the coupled thermal, mechanical and chemical phenomena in a fuel element under normal and/or accident conditions, represents a complex computational task and plays a central role in the development of modern fuel performance codes [1–5]. The large number of control parameters and the uncertainty associated with them leads often to challenging problems that can be addressed by a close integration of experimental, theoretical, and computational work [6–9].

Recently, we studied the nonlinear coupling between thermal, mechanical and chemical phenomena in a generic UO_2 fuel element, in order to elucidate general aspects of the fuel behavior in connection with the transport of the oxygen in the fuel element [10,11]. Our results indicate that the coupling between heat transport, oxygen diffusion, and thermal expansion in a fuel pellet can provide insight into the main mechanisms that cause fuel damage and allowed for the better understanding of the characteristic response times of the temperature, oxygen distribution and radial deformation profiles in the fuel element. We showed that following a sudden change in operating conditions, the characteristic time of thermal expansion is the same as the characteristic time for the transient response of the temperature profile in the fuel element. However, the characteristic response for heat and oxygen diffusion can be very different due to the large differences in the Lewis numbers. As a consequence, the non-stoichiometry and temperature/deformation evolve at different time scales and secondary transient responses in temperature/deformation can occur long after the early transient response. The dynamics of the characteristic times as a function of non-stoichiometry plays an important role in the transient behavior of oxide fuels.

In this paper we restrict our study to the case of a schematic model of a typical fuel element to develop the basic understanding of the underlying physics in connection with the nonlinear aspects of the coupled multi-physics phenomena involved. We focus on understanding the sensitivity of the simulation results in UO_{2+x} nuclear fuel elements to the choice of fuel thermal conductivity model. Hence, important aspects pertaining to the in-core behavior of the fuel element, such as irradiation-induced modifications of material properties, fuel swelling due to the accumulation of gaseous and solid fission products, fuel densification and creep, are intentionally left out here, but will have to be considered in realistic fuel-performance simulations [12–14].

2. Multiphysics model

Similarly to our previous work [10,11], we consider a schematic model for a UO_2 fuel pellet separated through a helium gap from a steel cladding (see Fig. 1). The computational domain consists of a

* Corresponding author.
E-mail address: bmihaila@lanl.gov (B. Mihaila).

0022-3115/$ - see front matter © 2012 Elsevier B.V. All rights reserved.
http://dx.doi.org/10.1016/j.jnucmat.2012.07.007

cylindrical fuel pellet of radius R_{fuel} = 4.3 mm, separated by a 0.03 mm width helium gap from a cylindrical cladding of thickness 0.5 mm. The geometry of the fuel element is depicted in Fig. 1. In this geometry we solve the coupled heat transport, oxygen diffusion and thermal expansion problem corresponding to an uniformly distributed source term, Q. The heat transport equation is given by

$$\rho\ C_P\ \frac{\partial T}{\partial t} = \nabla \cdot (k \cdot \nabla T) + Q, \tag{2.1}$$

where ρ, C_P and k are the density, specific heat at constant pressure and thermal conductivity, respectively. Because the oxide nuclear fuel is non-stoichiometric, all material properties of the fuel are in principle dependent on both the temperature, T, and the deviation from stoichiometry, x,

$$x = O/M - 2, \tag{2.2}$$

where O/M denotes the oxygen-to-metal ratio. Hence, the heat transport Eq. (2.1) must be solved self-consistently with the diffusion equation describing the oxygen transport in the fuel pellet. In order to model the oxygen transport in UO_{2+x} fuel elements, we assume without loss of generality, that hyper-stoichiometric systems are pseudo-binary systems described as dilute solutions of oxygen interstitials in the oxygen sublattice [16]. We consider the continuity equation,

$$n\frac{\partial c}{\partial t} = \nabla \cdot \mathbf{J}, \tag{2.3}$$

where c denotes the atomic fraction of oxygen interstitials and n is the total number of regular oxygen sites per unit volume. Based on thermodynamic considerations [17], the flux of oxygen interstitials is written as

$$\mathbf{J} = -n\ D\left(\nabla c + \frac{c}{F}\frac{Q^*}{RT^2}\nabla T\right), \tag{2.4}$$

where D is the chemical diffusion coefficient, Q^* is the heat of transport, F is the thermodynamic factor, and R is the ideal gas constant. In Eq. (2.4), the gradient of non-stoichiometry is associated with the conventional Fickian diffusion contribution, whereas the term involving a gradient in temperature represents the thermal segregation or the Soret effect [18]. In the dilute limit, $x \to 0$, the thermodynamic factor has the limit $F \to 1$.

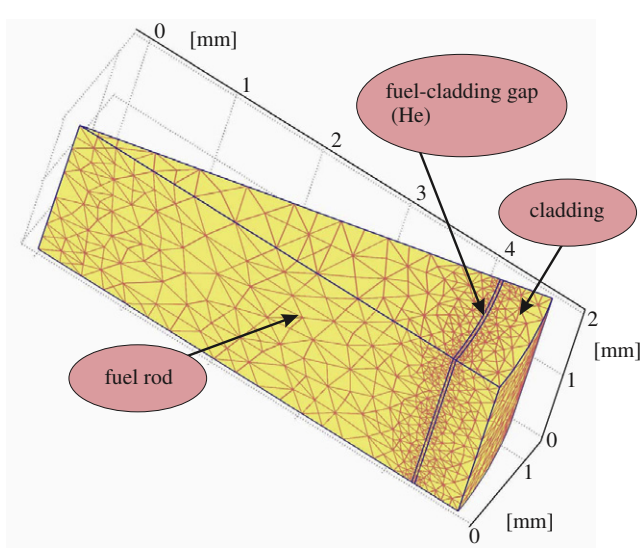

Fig. 1. Geometry of the fuel element.

For hyper-stoichiometric oxides, the atomic fractions, c, is related to the deviation from stoichiometry, x, as

$$x = c. \tag{2.5}$$

Therefore, for an arbitrary oxide MO_{2+x}, Eqs. (2.3) and (2.4) can be written in terms of the deviation from stoichiometry, x, as

$$n\ \frac{\partial x}{\partial t} = \nabla \cdot \mathbf{J}, \tag{2.6}$$

with

$$\mathbf{J} = -n\ D\left(\nabla x + \frac{x}{F}\frac{Q^*}{RT^2}\nabla T\right). \tag{2.7}$$

Eqs. 2.1, 2.3, and 2.7 are solved self-consistently. The ensuing distribution of temperature and compositions are used to calculate the mechanical deformation of the pellet and cladding. For simplicity, the pellet and cladding are considered as uniform, pure elastic materials, characterized by the Young's modulus, Poisson ration, thermal expansion coefficient, and density. This formulation accounts for the temperature and composition dependence of the mechanical properties.

The total strain tensor, ε, is written in terms of the gradient of the displacement, $\mathbf{u}$, as

$$\varepsilon = \frac{1}{2}\ (\nabla\mathbf{u} + \nabla\mathbf{u}^T). \tag{2.8}$$

The relationship between the stress tensor, σ, the strain tensor, ε, and temperature, T, is given by the Duhamel–Hooke's law, as

$$\sigma = \sigma_0 + C : [\varepsilon - \varepsilon_0 - \alpha(T - T_{ref})], \tag{2.9}$$

where C is the elasticity tensor, σ_0 and ε_0 are the initial stresses and strains, T_{ref} is the reference temperature, and α is the thermal expansion coefficient. The elasticity tensor, C, is given in terms of the Young's modulus, E, and the Poisson ratio, ν, as described for instance in Ref. [14].

The resulting system of equations for the thermo-mechanical model and oxygen diffusion, is solved using a fully-coupled direct solver in COMSOL.

3. Material properties

Properties of the materials in the fuel element were obtained from previously published correlations and are summarized in Tables 1–3, for helium, cladding, and UO_{2+x}, respectively. Given the schematic nature of this study, in this paper we use a 316 grade stainless-steel cladding material just like we did previously (see Ref. [14]).

For fuel-performance assessment purposes, one of the most important material property is the thermal conductivity of the fuel. This well-known fact was also emphasized in our analysis that emphasized the oxygen redistribution effects on the thermal response of the fuel element [10,11]. In order to get a better understanding of the margins of error in the thermal response due to uncertainties in the thermal conductivity of UO_{2+x}, in Table 4 we summarize the experimentally-based analytical models of thermal conductivity of UO_{2+x} considered in this study. The temperature dependence of these thermal conductivity models [22,19–27,30,31] for stoichiometric UO_2 is illustrated in Fig. 2 for a temperature range between 300 and 3000 K. Two of these models, i.e. the A96 model proposed by Amaya et al. [31] and the C01 model recommended by Carbajo et al. [27] include an explicit oxygen deviation from stoichiometry dependence, and are recommended from deviations lower than 0.2 and 0.1, respectively. The temperature dependence of the A96 and C01 UO_{2+x} thermal conductivity models for several deviations is illustrated in Fig. 3 for several deviations from stoichiometry in the range 0.0–0.1.

Table 1
Summary of the properties of the helium filling the gap in the fuel element depicted in Fig. 1. Here, ρ, C_P and k denote the density, heat capacity and thermal conductivity, respectively.

Property (material)	Functional form of the property on temperature, T	Units	Source
ρ (He)	$0.0818 - 8.275 \times 10^{-15}\,(T - 600)$	kg/m^3	[19]
C_P (He)	5190	J/(kg K)	[19]
k (He)	$0.04679 + 3.81 \times 10^{-4}T - 6.786 \times 10^{-8}T^2$	W/(m K)	[19]

Table 2
Summary of cladding material properties corresponding to the fuel element depicted in Fig. 1. In addition to the notations introduced in Table 1, we use α_T, E and ν to denote the thermal expansion coefficient, the Young's elasticity module and Poisson ratio, respectively. For convenience, the cladding is made out of the same 316 austenitic grade stainless-steel cladding material used in our previous work [11].

Property (material)	Functional form of the property on temperature, T	Units	Source
ρ (steel)	$7989 + 0.127T + 1.51 \times 10^{-5}T^2$	kg/m^3	[20]
C_P (steel)	$500 + 0.072T - 6.37 \times 10^{-4}T^2 + 1.73 \times 10^{-6}T^3$	J/(kg K)	[21]
k (steel)	$7.956 + 1.919 \times 10^{-2}T - 3.029 \times 10^{-6}T^2$	W/(m K)	[20]
α_T (steel)	$15.046 \times 10^{-6} + 5.082 \times 10^{-9}T - 1.014 \times 10^{-12}T^2$	m/(m K)	[20]
E (steel)	$211.622 \times 10^9 - 5.173 \times 10^7T - 1.928 \times 10^4T^2$	Pa	[20]
ν (steel)	0.29		[20]

Table 3
Summary of UO_{2+x} material properties. In addition to the notations introduced in Tables 1 and 2, we introduce $Q^{\star}$, F and D to denote the heat of transport, thermodynamic factor and chemical diffusion coefficient of oxygen in UO_2.

Property (material)	Functional form of the property on temperature, T, and non-stoichiometry, x	Units	Source
C_P ($UO_{2\pm x}$)	$a_0 + b_0x + (a_1 + b_1x)T + (1 - x)(a\,T^2 + b\,T^3 + c\,T^4) - (a_{-2} + b_{-2}x)T^{-2}$, with	J/(mol K)	[15]
	$a_0 = 52.174$, $b_0 = 45.806$,	J/(mol K)	
	$a_1 = 87.951$, $b_1 = -0.073461$,	J/(mol K^2)	
	$a = -84.241 \times 10^{-6}$,	J/(mol K^3)	
	$b = 31.542 \times 10^{-6}$,	J/(mol K^4)	
	$c = -2.6334 \times 10^{-12}$	J/(mol K^5)	
	$a_{-2} = 7.1391 \times 10^5$, $b_{-2} = 2.9509 \times 10^5$,	J K/mol	
ρ (UO_2)	$10970(a + bT + cT^2 + dT^3)^{-3}$, with	kg/m^3	[22,23]
	$\left.\begin{array}{l} a = 0.99734, b = 9.802 \times 10^{-6}, \\ c = -2.705 \times 10^{-10}, d = 4.391 \times 10^{-13} \end{array}\right\}$, for $T \leqslant 923$ K,		
	$\left.\begin{array}{l} a = 0.99672, b = 1.179 \times 10^{-5}, \\ c = -2.429 \times 10^{-9}, d = 1.219 \times 10^{-12} \end{array}\right\}$, for $T > 923$ K.		
	$a + bT + cT^2 + dT^3$, with	m/(m K)	[22,23]
	$\left.\begin{array}{l} a = 9.828 \times 10^{-6}, b = -6.390 \times 10^{-10}, \\ c = 1.33 \times 10^{-12}, d = -1.757 \times 10^{-17} \end{array}\right\}$, for $T \leqslant 923$ K,		
	$\left.\begin{array}{l} a = 1.1833 \times 10^{-5}, b = -5.013 \times 10^{-9}, \\ c = 3.756 \times 10^{-12}, d = -6.125 \times 10^{-17} \end{array}\right\}$, for $T > 923$ K.		
E (UO_{2+x})	$2.334 \times 10^{11}\,(1 - 1.095 \times 10^{-4}T)\exp(-1.34x)$	Pa	[26]
ν (UO_2)	0.316		[26]
$Q^{\star}$ (UO_{2+x})	$-1380.8 - 1.344 \times 10^5\exp(-x/0.0261)$	J/mol	[10]
F (UO_{2+x})	$(2 + x)/[2(1 - 3x)(1 - 2x)]$		[10,24]
D (UO_2)	$10^{-9.386-4.26\times10^3/T+1.2\times10^{-3}\ T1\ x+7.5\times10^{-4}\ T\ \log[(2+x)/x]}$	m^2/s	[10]

The thermal conductivity proposed by Amaya et al. [31] is based on the Klemens thermal conductivity model [32,33] based on the quantum theory of phonon–phonon and phonon-impurity interactions in solids. With this exception, all other thermal conductivity models are given as the sum of a lattice phonon contribution

$$k_{\mathrm{L}}(T, x) = \frac{1}{A(x) + C(x)t}, \tag{3.1}$$

and a small-polaron ambipolar term,

$$k_{\mathrm{AP}}(T) = \beta\, t^{-\gamma} \exp(-\delta/t), \tag{3.2}$$

where $t = T(K)/1000$. The effect of the deviation from stoichiometry, x, on the UO_{2+x} thermal conductivity is important only in the lattice part of the thermal conductivity [28]. The ambipolar term is designed to fit the high temperature data in UO_{2+x} and shows no dependence on x [30]. The inverse power-law coefficient, γ, is 2 in the work of Harding and Martin [25] and in MATPRO [26]. For consistency with the non-adiabatic nature of the hopping transport in which the small polarons participate [29], modern thermal conductivity models use a value $\gamma = 5/2$ following the analysis of Ronchi et al. [30].

The change in the thermal conductivity due to the porosity effect is calculated by multiplying the conductivity of the solid by the Maxwell–Eucken function

$$f_\sigma(p) = \frac{1 - p}{1 + (\sigma - 1)p}. \tag{3.3}$$

Here, p is the fractional porosity, with $p < 0.2$, and σ is a porosity shape factor. For spherical pores, the shape factor is $\sigma_0 = 1.5$. For flatter pores, we have $\sigma > \sigma_0$, whereas for tubular porosity, the porosity shape factor is $\sigma < \sigma_0$ [28]. We note that MATPRO assumes that the pores are spherical [26], whereas the prevalent recommended value is $\sigma = 3$ [22]. The simulations discussed in this paper assume a 96.5% dense fuel pellet.

For completeness, we note that the UO_2 density and thermal expansion coefficient used in our simulations are those reported

Table 4
Summary of UO_{2+x} thermal conductivity, k (UO_{2+x}), material models. Here we introduced the notation $t = T/1000$ with T measured in K.

Model (material)	Porosity	Functional form of the thermal conductivity	Units	Source
A96 (UO_{2+x})	0.035	$\lambda_0(T)\tan^{-1}[\theta(T,x)]/\theta(T,x) + 5.95 \times 10^{-11}T^3$, with $\lambda_0(T) = [3.24 \times 10^{-2} + 2.51 \times 10^{-4}T]^{-1}$, $\theta(T,x) = 3.67\ \exp(-4.73 \times 10^{-4}\ T)\sqrt{2x\ \lambda_0(T)}$.	W/(m K) W/(m K)	[31]
H89 (UO_2)	0.000	$[A + C\ t]^{-1} + 4715t^{-2}\exp(-16.361/t)$, with $A = 0.0375$ $C = 0.2165$	W/(m K) m K/W m/W	[25]
MATPRO (UO_2)	0.050	$[A + C\ t]^{-1} + 3500t^{-2}\exp(-16.361/t)$, with $A = 0.0452$ $C = 0.246$	W/(m K) m K/W m/W	[26]
R99 (UO_2)	0.050	$[A + C\ t]^{-1} + 6400t^{-5/2}\exp(-16.35/t)$, with $A = 0.06548$ $C = 0.23533$	W/(m K) m K/W m/W	[29]
F00 (UO_2)	0.050	$[A + C\ t + C't^2]^{-1} + 6400t^{-5/2}\exp(-16.35/t)$, with $A = 0.075408$ $C = 0.17692$ $C' = 0.036142$	W/(m K) m K/W m/W m/(K W)	[22]
C01 (UO_{2+x})	0.000	$[A(x) + C(x)t]^{-1} + 7410.53t^{-5/2}\exp(-16.35/t)$, with $A(x) = 0.0257 + 3.336x$ $C(x) = 0.2206 - 0.685x$	W/(m K) m K/W m/W	[27]

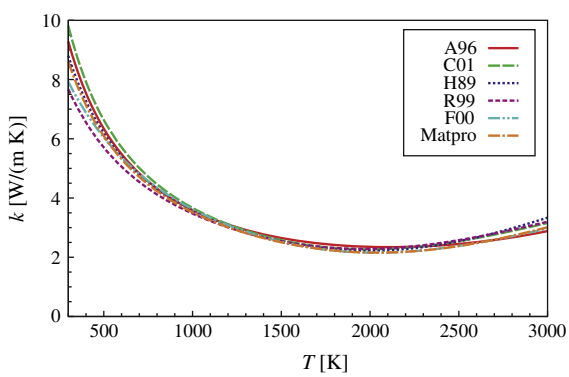

Fig. 2. Temperature dependence of the thermal conductivity models for stoichiometric UO_2 considered in this study.

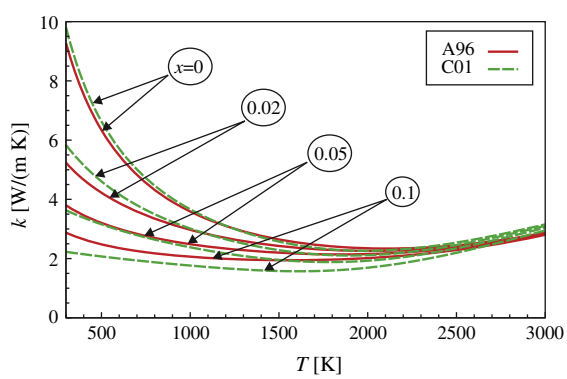

Fig. 3. Stoichiometry dependence of thermal conductivity models for UO_{2+x} considered in this paper.

by Martin [23], who showed that these material properties are largely insensitive to stoichiometry effects. We use the same UO_{2+x} heat capacity correlation as Higgs et al. [15].

4. Results and discussions

Solutions of the coupled multi-physics problem in the fuel, gap, and cladding are obtained by solving self-consistently Eq. (2.1) for the temperature, T, profile in the fuel, helium gap and steel cladding, together with the oxygen deviation from stoichiometry, x, given by Eqs. (2.6) and (2.7), in the fuel. The fuel pellet and steel cladding are allowed to expand freely in the radial direction at the expense of the gap. A moving mesh application in the Lagrangian–Eulerian formulation is used to account for the changing gap size with thermal expansion of the fuel and the clad. The heat transport in the gap is approximated using an effective thermal conductivity.

All simulations were performed using the commercial finite-element code COMSOL MultiphysicsTM. The heat transport was modeled using the heat-transport by conduction component of the Heat Transfer Module in COMSOL, whereas the thermal deformation was calculated using the plane strain component of the Structural Mechanics Module. For our simple geometry, we use the plane strain application of the structural mechanics module in static or transient regime, as appropriate. We used symmetric boundary conditions for solid mechanics, T, and x along the straight edges of the fuel element (see Fig. 1). The linear solver of choice is the default non-symmetric multi-frontal method (UMFPACK) in COMSOL. The finite-elements mesh generated in COMSOL uses quadratic Lagrange elements and the results presented here were converged with respect to the mesh-size distribution.

In the following, we consider the case of Dirichlet (fixed-value) boundary conditions for both the temperature at the cladding outer surface, T_b, and the deviation from stoichiometry at the fuel pellet outer surface, x_b. We emphasize that the simulations discussed here are intended as basic illustrations of fundamental principles. In more realistic simulations [15], one should consider important phenomena such as the fuel/steam reaction rate at the pellet surface [34] and the gas phase transport through fuel cracks.

We begin by considering the case of steady-state simulations. In this case, the temperature and composition do not depend on time, and the left-hand-sides of Eqs. (2.1) and (2.3) are equal to zero. Hence, the flux of oxygen atoms vanishes ($J = 0$) everywhere in the fuel pellet and the steady-state solution is independent of the oxygen diffusivity.

For illustrative purposes, we fix $T_b = 750$ K and study the changes in the profiles of temperature, composition and radial displacement in the fuel pellet as a function of x_b. Results obtained for the UO_2 thermal conductivity models summarized in Table 4 and two values of the heat-generation rate, $Q = 2 \times 10^7$ W/m^3 and $Q = 2 \times 10^8$ W/m^3, are depicted in Figs. 4 and 5, respectively. We

notice that predictions for the temperature and radial deformation profiles in the fuel corresponding to thermal conductivity models that do not account for the non-stoichiometry dependence (i.e. $k(T)$) lie in a narrow band, independent of the composition of the fuel. This "band" also contains results obtained using the thermal conductivity models for stoichiometric fuel composition, consistent with the temperature-dependence of the thermal conductivity models $k(T, x)$ depicted in Fig. 2. The results for the fuel temperature and radial deformation profiles change dramatically from the stoichiometric baseline as a function of x_b, provided that the heat transport and oxygen diffusion are coupled using a stoichiometry-dependent thermal conductivity model. The changes relative to the stoichiometric baseline are enhanced by larger values of x_b, and larger heat-generation rates, Q. We note that the predictions corresponding to the A96 and C01 models are close for small value of x_b but these differences are considerable for larger values of x_b. This findings are in contrast with the relatively small differences between these two thermal conductivity models depicted in Fig. 3 and are due to the nonlinear character of the heat transport and oxygen diffusion coupling. The radial oxygen composition profiles shown in Figs. 4 and 5 as a function of x_b indicate that the heat transport and oxygen diffusion coupling is weak at large values of x_b.

Next, we consider the case of transient simulations driven by a rapid change in the heat-generation rate, Q, or the boundary-condition value for the non-stoichiometry at the outer surface of the fuel pellet, x_b. In the first two scenarios $Q(t)$ starts out at an initial value, Q_0, and quickly (within 10 min) reaches a value Q_{max} according to the equation

$$Q(t) = Q_0 + \frac{Q_{max} - Q_0}{1 + 10\ \exp[-(-10 + t/\tau)]}, \tag{4.1}$$

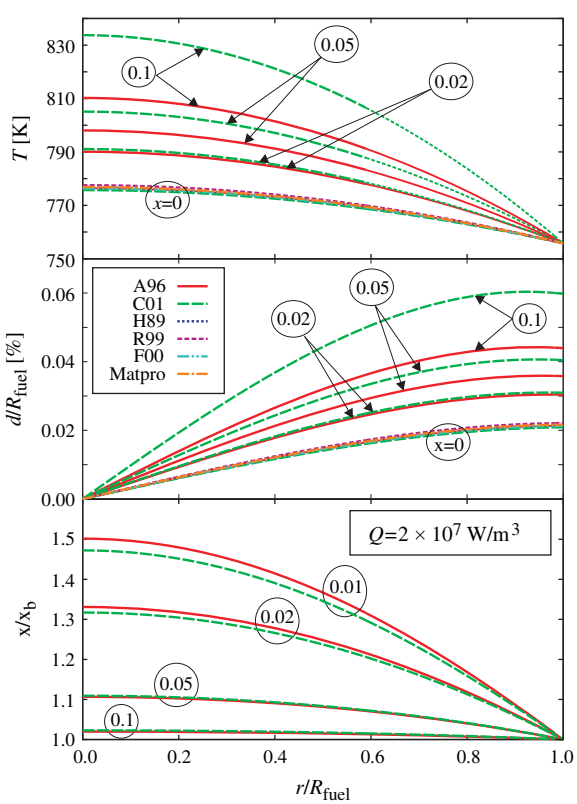

Fig. 4. Steady-state radial profiles of the temperature, T, total radial displacement, d, and deviation from stoichiometry, x, for a heat-generation rate, $Q = 2 \times 10^7$ W/m^3. In these simulations we chose a temperature boundary condition, $T_b = 750$ K, and several values of the non-stoichiometry boundary condition, x_b.

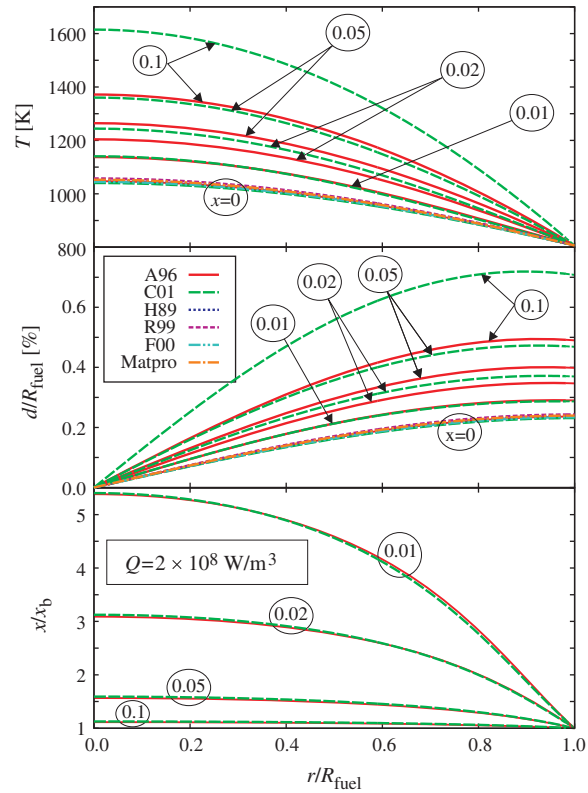

Fig. 5. Steady-state radial profiles of the temperature, total radial displacement and non-stoichiometry for a heat-generation rate, $Q = 2 \times 10^8$ W/m^3. In these simulations the temperature boundary condition is $T_b = 750$ K, and we choose several values of the non-stoichiometry boundary condition, x_b.

where $\tau = 45$ s is a time constant. In a third scenario, x_b changes according to the equation

$$x_b(t) = x_{b,0} + \frac{x_{b,max} - x_{b,0}}{1 + 100\exp[-(-5 + t/\tau)]}, \tag{4.2}$$

where $x_{b,0}$ and $x_{b,max}$ are the initial and final values, respectively, of x_b. These scenarios are only intended to evaluate the predictions of our simulations.

As discussed in our previous studies [10,11], the characteristic times for the fuel pellet deformation, together with the characteristic time of heat and oxygen diffusion, determine the time required for the equilibration of reactor parameters following a change in operating conditions. The equilibration time scales for the radial deformation in the fuel pellet generally matches the equilibration time scale of the temperature profile in the fuel, whereas the times scales for the equilibration of the composition and temperature profiles can be vastly different. The relative difference in the time scales for heat transport and oxygen diffusion is characterized by the Lewis number, $\mathrm{Le}(T, x) = \alpha(T, x)/D(T, x)$, which represents the ratio of the time required by the deviation from stoichiometry field, x, to reach a steady state, to the time required for the temperature field, T, to reach a steady state. Here $\alpha = k/(\rho C_P)$ is the thermal diffusivity in UO_{2+x}. The Lewis number can be much larger than 1 for strongly non-stoichiometric fuel pellets at low temperatures, which implies that changes in the temperature distribution can occur with negligible changes in the non-stoichiometry distribution.

In Figs. 6 and 7, we depict the results corresponding to a start-up reactor scenario. In this case, the heat-generation rate varies from a zero initial value $Q_0 = 0$ to a final value $Q_{max} = 2 \times 10^8$ W/m^3, according to Eq. (4.1). Similarly, in Figs. 8 and 9, we show re-

sults corresponding to a time-dependent heat-generation scenario with the heat-generation rate varying from an initial value $Q_0 = 2 \times 10^7$ W/m^3 to a final value $Q_{max} = 2 \times 10^8$ W/m^3, according to Eq. (4.1). In both cases, the temperature at the outer surface of the steel cladding is fixed to the initial temperature, $T_b = T_0 = 750$ K. We consider two separate Dirichlet boundary conditions $x_b = 0.01$ and $x_b = 0.1$. In the time-dependent heat-generation rate scenario, the initial conditions are set by solving the steady-state problem for a fuel pellet with a non-stoichiometry at the outer edge, $x_b = 0.01$ and $x_b = 0.1$ and the initial heat-generation rate, $Q = 2 \times 10^7$ W/m^3.

Similar to the situation observed in our steady-state simulations discussed above, the results of simulations using composition-independent thermal conductivity $k(T)$ models lie in a narrow band. The differences in the deformation, temperature and non-stoichiometry profiles induced by the different thermal conductivity models are significantly smaller than the differences due to the inclusion of stoichiometry-dependent thermal conductivity $k(T, x)$ models. This effect is magnified by a larger value of x_b. In all cases, we notice that the time evolution of the centerline temperature, T_0, and radial total displacement at the surface of the pellet closely track each other, in response to a change in the heat-generation rate. In contrast, the equilibration of the centerline deviation from stoichiometry, x_0, lags behind the evolution of the centerline temperature for $k(T, x)$ models as the characteristic time associated with oxygen diffusion is much larger than the heat transport characteristic time. This results in a second transient response in the centerline temperature and the total displacement at the outer edge of the fuel pellet that coincides with the centerline non-stoichiometry value reaching its equilibrium value. The magnitude of the secondary transient response is larger for smaller x_b

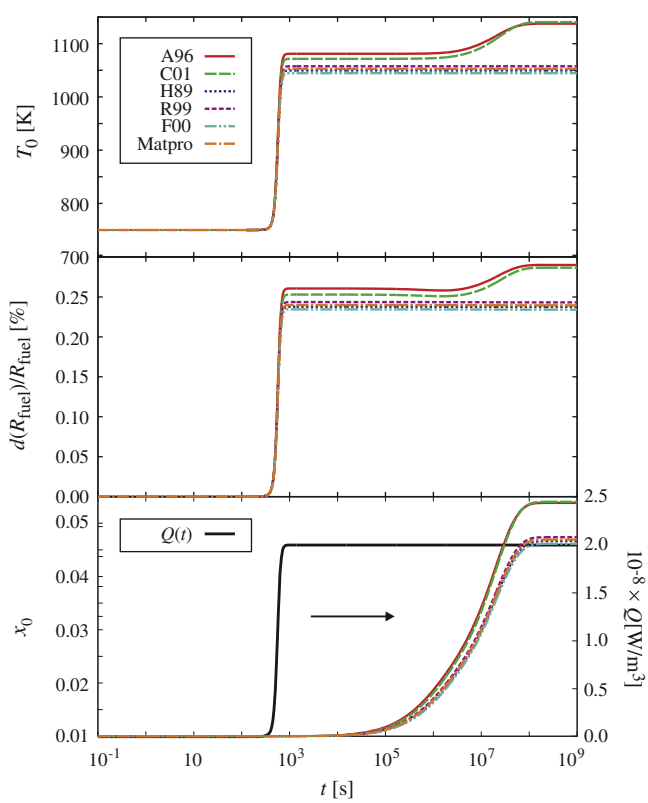

Fig. 6. Results of transient simulations for a start-up reactor scenario. We illustrate the time evolution of the centerline temperature, T_0, total radial displacement of the outer surface of the fuel pellet, $d(R_{fuel})$, and centerline deviation from stoichiometry, x_0. Here, we consider Dirichlet boundary conditions for temperature, $T_b = 750$ K, and composition, $x_b = 0.01$.

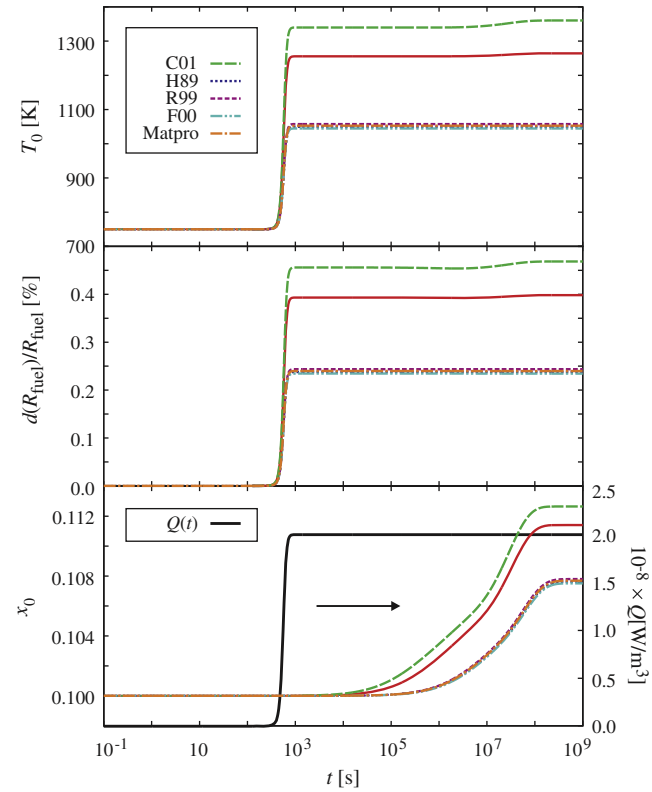

Fig. 7. Results of transient simulations for a start-up reactor scenario. Here, we consider Dirichlet boundary conditions for temperature, $T_b = 750$ K, and composition, $x_b = 0.1$.

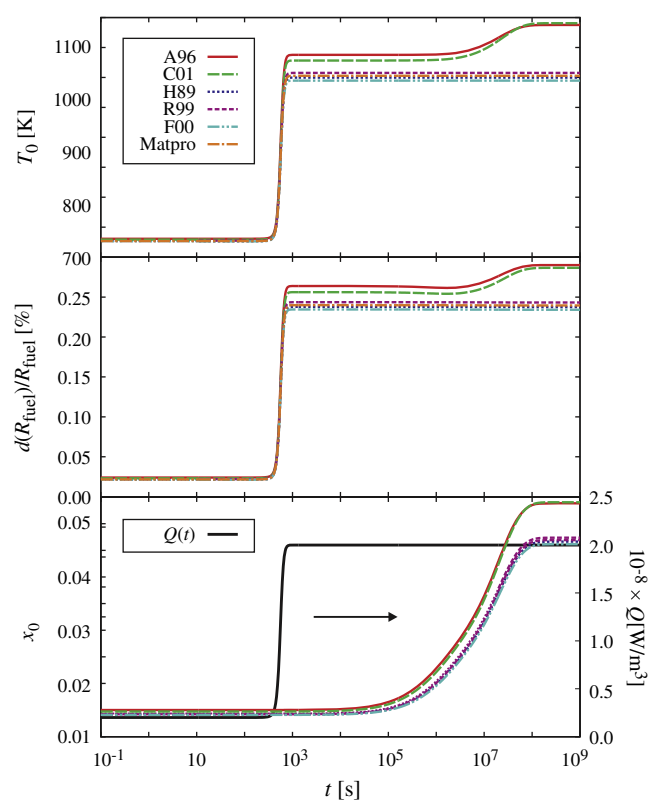

Fig. 8. Results of transient simulations for a heat-generation scenario. Here, we consider Dirichlet boundary conditions for temperature, $T_b = 750$ K, and composition, $x_b = 0.01$.

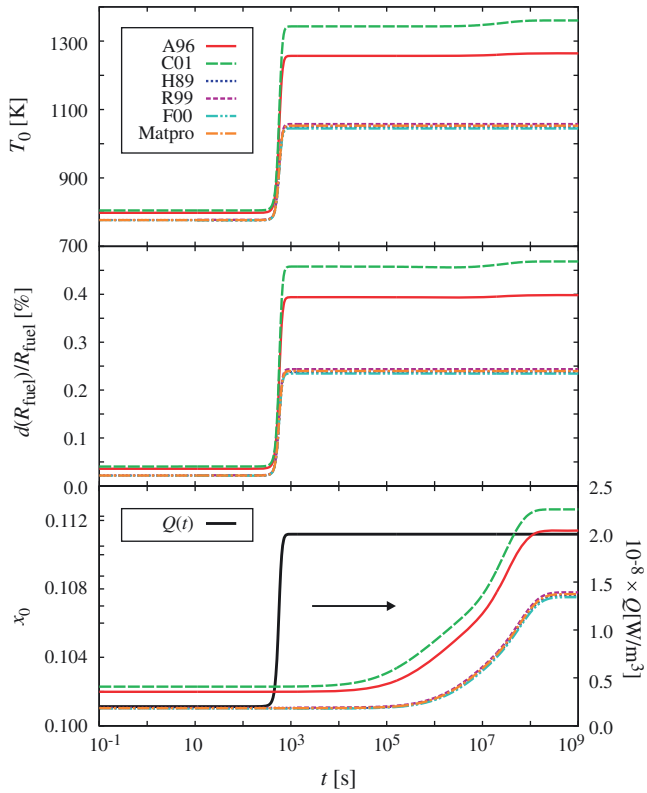

Fig. 9. Results of transient simulations for a heat-generation scenario. Here, we consider Dirichlet boundary conditions for temperature, $T_b = 750$ K, and composition, $x_b = 0.1$.

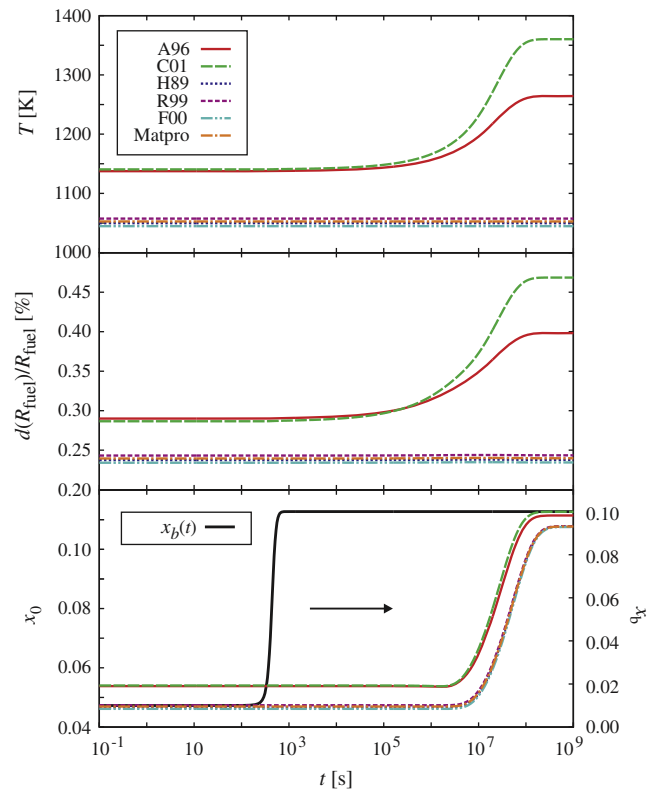

Fig. 10. Results of transient simulations for a time-dependent non-stoichiometry boundary conditions scenario. Here we consider Dirichlet boundary conditions for temperature, $T_b = 750$ K, and a heat-generation rate, $Q = 2 \times 10^8$ W/m^3.

values, indicative of a stronger coupling between heat transport and oxygen diffusion for smaller values of x_b. This result is consistent with our findings in the steady-state case. Finally, the differences between the predictions corresponding to the A96 and C01 $k(T, x)$ models are larger for larger values of x_b, similarly to what was observed in the stead-state simulations described above.

Finally, in Fig. 10, we show results corresponding to a time-dependent non-stoichiometry Dirichlet boundary condition at the outer surface of the fuel pellet x_b. In this simulation we fix the temperature at the outer face of the steel cladding, $T_b = 750$ K and the heat-generation rate is constant, $Q = 2 \times 10^8$ W/m^3. The non-stoichiometry at the outer face of the fuel pellet, x_b, changes according to Eq. (4.2) from an initial value $x_{b,0} = 0.01$ to a final value $x_{b,max} = 0.1$ over the course of approximately 10 min. This scenario corresponds to having the state of the fuel element transition between the $x_b = 0.01$ and $x_b = 0.1$ profiles calculated for $Q = 2 \times 10^8$ W/m^3 shown in Fig. 5. Similarly to the time-dependent heat-generation rate scenarios, the time evolution of the total radial displacement due to thermal expansion follows the time evolution of the temperature. In contrast with that type of scenario, the results in Fig. 10 show that the non-stoichiometry profile in the fuel element is expected to react slowly to the change in the boundary condition, reflecting the large time scales associated with oxygen diffusion. Unlike the time-dependent heat-generation rate scenario, in this case the time scale of the changes in temperature, non-stoichiometry and deformation are controlled by the time scale of the oxygen diffusion process, and we do not observe the secondary transients in Figs. 6–9. The sensitivity of the simulation results to the choice of fuel thermal conductivity model is consistent with what was observed above. For thermal conductivity models that are composition independent, $k(T)$, results lie in a narrow band, these differences being dwarfed by the changes induced by composition effects as in $k(T, x)$. The importance of the deviation in stoichiometry effects is already responsible for ~100 K change in the centerline temperature in the initial state (small deviation, $x_b = 0.01$). This change in the centerline temperature becomes at least 200 K in the final state (large deviation, $x_b = 0.1$). For small x_b values, the two stoichiometry-dependent models, A96 and C01, give rise to very similar predictions, whereas for the large non-stoichiometries ($x_b = 0.1$) the C01 model predicts an additional 100 K increase in the centerline temperature relative to the A96 model.

5. Conclusions

In this paper we study the impact of different thermal conductivity models on the thermal response and the radial fuel deformation of a generic UO_2 fuel element using multi-physics simulations of coupled thermal transport, oxygen diffusion, and thermal expansion. A series of steady-state and time-dependent finite-element simulations with a variety of initial-value conditions show that including the deviation from stoichiometry, x, in the thermal conductivity model, $k(T, x)$, results in significant changes in the evaluation of the centerline temperature T_0 and the extent of the radial deformation of the fuel pellet, compared with simulations that do not account for oxygen content.

We find that solving for the thermo-mechanical response together with the oxygen diffusion in the pellet is important for accurate fuel performance studies at all oxygen compositions in the fuel. The coupling between the heat transport and the oxygen diffusion is stronger for small deviations from the fuel stoichiometry. The coupling becomes weak for large deviations from stoichiometry.

Our simulations indicate that relatively small differences in the $k(T, x)$ values of the A96 and C01 models give rise to significant differences in the predicted temperature profiles, with the C01 model generally leading to larger centerline temperatures compared to the A96 model.

Acknowledgments

This work was performed under the auspices of the United States Department of Energy. BM gratefully acknowledges partial financial support from the Consortium for Advanced Simulation of Light Water Reactors (www.casl.gov), an Energy Innovation Hub (http://www.energy.gov/hubs) for Modeling and Simulation of Nuclear Reactors under US Department of Energy Contract No. DE-AC05-00OR22725. MS research is supported by the US Department of Energy, Office of Science under Contract No. DE-AC02-06CH11357.

References

[1] H.S. Aybar, P. Ortego, Prog. Nucl. Energy 46 (2005) 127.
[2] J.R. Matthews, Bull. Mater. Sci. 8 (1986) 93.
[3] M.R. Tonks, D. Gaston, P.C. Millett, D. Andrs, P. Talbot, Comp. Mater. Sci. 51 (2012) 20.
[4] M.H.A. Piro, T.M. Besmann, S. Simunovic, B.J. Lewis, W.T. Thompson, J. Nucl. Mater. 414 (2011) 399.
[5] B.-H. Lee, Y.-H. Koo, J.-Y. Oh, J.-S. Cheon, D.-S. Sohn, Nucl. Technol. 157 (2007) 53–64.
[6] B. Dorado, P. Garcia, G. Carlot, C. Davoisne, M. Fraczkiewicz, B. Pasquet, M. Freyss, C. Valot, G. Baldinozzi, D. Simeone, M. Bertolus, Phys. Rev. B 83 (2011) 035126.
[7] E.C. Corcoran, B.J. Lewis, W.T. Thompson, J. Mouris, Z. He, J. Nucl. Mater. 414 (2011) 73.
[8] M. Stan, J. Nucl. Eng. Technol. 41 (2009) 39.
[9] M. Stan, Mater. Today 12 (2009) 20.
[10] J.C. Ramirez, M. Stan, P. Cristea, J. Nucl. Mater. 359 (2006) 174.
[11] B. Mihaila, M. Stan, J.C. Ramirez, A. Zubelewicz, P. Cristea, J. Nucl. Mat. 394 (2009) 182.
[12] J.D. Higgs, B.J. Lewis, W.T. Thompson, Z. He, J. Nucl. Mater. 366 (2007) 99.
[13] B.J. Lewis, W.T. Thompson, F. Akbari, D.M. Thompson, C. Thurgood, J. Higgs, J. Nucl. Mater. 328 (2004) 180.
[14] C. Newman, G. Hansen, D. Gaston, J. Nucl. Mater. 392 (2009) 6.
[15] J.D. Higgs, B.J. Lewis, W.T. Thompson, D.M. Thompson, Z. He, J. Nucl. Mater. 366 (2007) 99.
[16] C. Sari, G. Schumacher, J. Nucl. Mater. 61 (1976) 192.
[17] S.R. De Groot, Thermodynamics of Irreversible Processes, North Holland Publ., Co., Amsterdam, 1951.
[18] C. Korte, J. Janek, H. Timm, Solid State Ionics 101/103 (1997) 465.
[19] A. Bejan, Heat Transfer, first ed., John Wiley & Sons, New York, 1993.
[20] C. Basavaraju, 2004 ASME Pressure Vessels and Piping Conference, 2004.
[21] Michael Bauccio (Ed.), ASM Metals Reference Book, third ed., ASM, Materials Park, OH, 1993.
[22] J.K. Fink, J. Nucl. Mater. 279 (2000) 1.
[23] D.G. Martin, J. Nucl. Mater. 152 (1988) 94.
[24] T.B. Lindemer, T.M. Besmann, J. Nucl. Mater. 130 (1985) 473.
[25] J.H. Harding, D.G. Martin, J. Nucl. Mater. 166 (1989) 166.
[26] D.T. Hagrman (Ed.), CDAP/RELAP5/MOD3.1 Code Manual, Volume IV: MATPRO – A Library of Materials Properties for Light-Water-Reactor Accident Analysis, NUREG/CR-6150, EGG-2720 Volume IV, 1993.
[27] J.J. Carbajo, G.L. Yoder, S.G. Popov, V.K. Ivanov, J. Nucl. Mater. 299 (2001) 181.
[28] P.G. Lucuta, Hj. Matzke, I.L. Hastings, J. Nucl. Mater. 232 (1996) 166.
[29] M. Sheindlin, D. Halton, M. Musella, C. Ronchi, Rev. Schi. Instrum. 69 (1998) 1426.
[30] C. Ronchi, M. Sheindlin, M. Musella, G.J. Hyland, J. Appl. Phys. 85 (1999) 776.
[31] M. Amaya, T. Kubo, Y. Korei, J. Nucl. Sci. Technol. 33 (1996) 636.
[32] P.G. Klemens, Proc. Phys. Soc. A68 (1955) 1113.
[33] P.G. Klemens, Phys. Rev. 119 (1960) 507.
[34] D.R. Olander, Y.S. Kim, W.E. Wang, S.K. Yagnik, J. Nucl. Mater. 270 (1999) 11.